Power Electronic Drivers for Electrostatic HASEL Actuators Used in Soft Mobile Robots

Tirthasarathi Lodh, *Student Member, IEEE* and Hanh-Phuc Le, *Senior Member, IEEE*

***Abstract*—This paper proposes, analyzes, designs, and validates topologies of dual coupled inductor hybrid (DCIH) converters that are capable of supporting enormous conversion ratios up to ∼2700X and output voltage up to ∼4-9 kV from a very low voltage supplied by a 1-cell battery pack for the standalone electromechanical energy conversion devices called soft robots made out of HASEL (Hydraulically Amplified Self-healing Electrostatic) actuators. A unique hybrid combination of pulse current sources (PCSos) and a 12-diode, Negative output, X (X is L for Ladder, M for Mixed, or D for Dickson) type, Diode-Capacitor-based Voltage Multiplier Rectifier (12N(X)DCVMR) helps to achieve small overall size, efficient operation, output voltage regulation, and shaping with simple duty-cycle modulation, which makes them promising candidates for future untethered soft robots. One of the illustrated operating points by the proposed DCIH converter has an input voltage of 3.3 V, an output voltage of 9 kV, at 16.2 W output with an efficiency of 75 %, and a power density of 10 W/in^3.**

***Keywords*—Hybrid converter, actuator, soft robot, energy conversion, high voltage gain, voltage multiplier.**

NOMENCLATURE

CCM: Continuous Conduction Mode
DCIH: Dual Coupled Inductor Hybrid
DCM: Discontinuous Conduction Mode
DCVMR: Diode and Cap. based Voltage Multiplier Rectifier
HASEL: Hydraulically Amplified Self-healing Electrostatic
HVW: High Voltage Winding
LVW: Low Voltage Winding
PCSo: Pulsed Current Source
TN(X)DCVMR: T- No. of Diodes, N- Negative circuit, X- type of DCVMR. Here X can be either L (for Ladder), M (for Mixed), or D (for Dickson)

I. INTRODUCTION

HASEL (Hydraulically Amplified Self-healing Electrostatic) [1], [2] and associated soft robots are well-suited for applications like the aerospace, automotive, deep sea, defense, human-machine interface, industrial automation, medical devices, and consumer products [3]. HASEL is a superior soft robotic actuator for numerous reasons. HASEL actuators are electrostatically powered, preferably by batteries for untethered mobility. HASEL actuators consist of three parts. A conductive and safe carbon-based substance forms its electrodes. Their pouch is formed by a flexible, soft, and thin thermoplastic polymer film. Their liquid dielectric is a transformer oil or vegetable. oil, making them very cost-effective. Due to liquid dielectrics and thin polymer sheets, HASEL actuators are exceedingly compliant, malleable, and lightweight. HASEL actuators operate with turn-on times as low as 10 mS and operating frequencies into the hundreds of Hz thanks to the electric control. Because HASEL actuators are capacitive, it is possible to utilize a simple impedance signal to check the actuator's physical condition continuously [4], [5]. The absence of pneumatic tubing, valves, compressors, large motors, or metal parts keeps the operation of HASEL quiet. Actuators made of HASEL have shown lifetimes of up to millions of cycles. Since HASEL actuators are electrically powered, they may be transported quickly, thanks to a battery-powered power source. HASEL actuators can move very organic and lifelike because of analog motion, electrical driving, and compliant constructions. Actuators from HASEL are modular.

TABLE I
COMPARISON WITH COMPACT, HIGH GAIN CONVERTERS

Conv.	Sw.	Di.	Cap.	Wdg.	V_{bat}	V_o (V)	Gain	Act.
This	4	14	12	4	3.4 V	9000	2700	Yes
[6]	2	2	3	2	24 V	250	8	No
[7]	2	6	5	4	40 V	380	9.5	No
[8]	4	4	5	5	40 V	380	9.5	No
[9]	1	3	3	2	25 V	200	8	No
[10]	2	1	2	2	25 V	200	8	No

*Column "Act." stands for whether the circuit can actuate a soft robot made out of HASEL actuators

TABLE II
COMPARISON WITH HIGH-OUTPUT VOLTAGE AND HIGH-GAIN COMMERCIALLY AVAILABLE PRODUCTS

Conv. Capabilities	[11]	[12]	[13]	[14]	[15]	This
Gain	2k	2k	2k	1.2k	1-2k	1-3k
Max. Op. Volt. (kV)	10	10	10	6	5	9
Efficiency	0.7	0.75	N/A	N/A	0.75	0.75
Max. Op. Pow. (W)	1.25	5	0.5	1	15	25
Pow. Density (W/in^3)	5	3.94	0.8	6.67	2.5	10
Weight (g)	9.5	45	4.25	8.49	120	120
Pow. Density (W/g)	0.13	0.11	0.12	0.12	0.13	0.2
Cost (USD)	382	400	290	240	112	65
Waveform synthesis	No	No	No	No	No	Yes

* [11]-PICO 5AVP10K; [12]-PICO 5VV10-P; [13]-EMCO Q101; [14]-XP Power AG60P-5

The article in [1] explains the construction and the electromechanical energy conversion principle of HASEL in detail. More strain for the same load is obtained when many actuators are layered on top of one another. The actuator can lift a higher load when a higher voltage is used. Not only high voltage, high power ($\geq$ 5 W) is also an essential requirement to support larger systems with larger payloads and enable a soft robot to respond quickly [16], [17]. The adjustable output voltage is essential to support a range of actuators and actuation strengths. An extremely high conversion ratio is required to

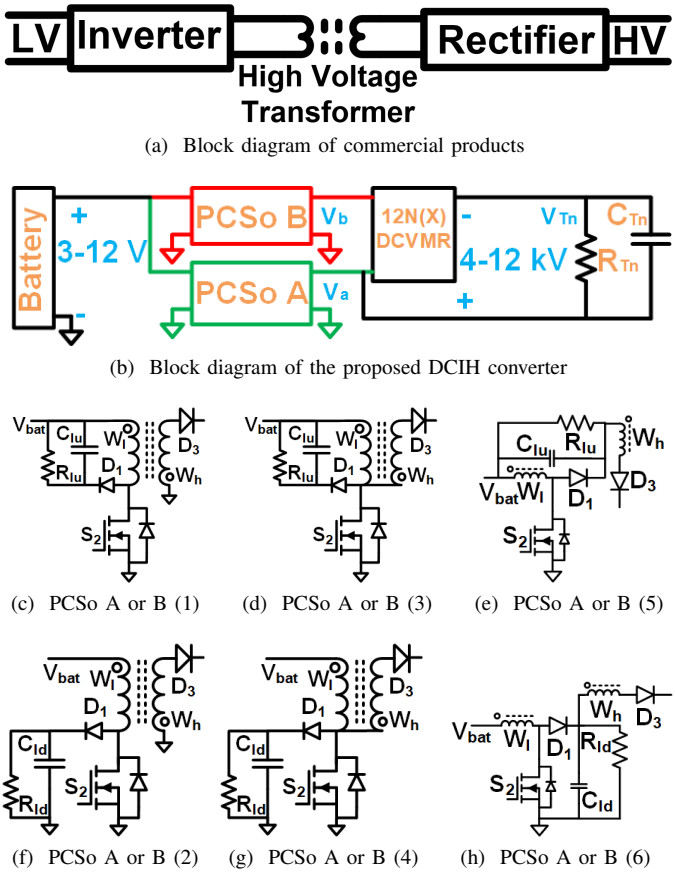

(a) Block diagram of commercial products

(b) Block diagram of the proposed DCIH converter

(c) PCSo A or B (1) (d) PCSo A or B (3) (e) PCSo A or B (5)

(f) PCSo A or B (2) (g) PCSo A or B (4) (h) PCSo A or B (6)

Fig. 1. Proposed PCSo B which goes into fitted in Fig.1b

make the overall system light and support untethered operation by deriving the power from a low-voltage Li-ion battery. This work focuses on achieving all these requirements with low cost, low volume, lightweight, modular, and efficient circuits.

The high-gain converters demonstrated in the literature [8]–[10], [18], [19] and the work included in Tab. I are not suitable for driving HASEL actuators for soft robots because their output voltage is limited to a few 100s of volts, nor able to be powered from LV batteries because their gain is limited to a few 10s times. Even though the available commercial products [11]–[14] provide high voltage, they either suffer from a low power or large size or do not have programmable output voltage capability.

In Tab. II, commercial products are listed. Some of them can output 10 kV from 5 V input; one can output 6 kV only. One limitation of all these converters is that their max output power is only limited to 5 W or much lesser. It is lower than the requirement for a soft robot made of HASEL. Moreover, due to their low power density, it's hard to integrate these power converters with mobile soft robots. Third, their low efficiency will lead to either a larger battery pack or less run time. Last, none of them has regulations. All these products have a fundamental circuit structure shown in Fig. 1a. The inverter changes the DC input to an AC signal. Then the high-voltage transformer provides the step-up conversion of the AC voltage. It has a fixed conversion ratio determined by its turns ratio. The transformer can be bulky to deliver high output power; therefore, these products do not have high power density. At the last stage, a conventional full bridge rectifier would rectify the output high voltage AC signal from the transformer and generate the high voltage DC output.

To achieve the goal of higher output power while maintaining a small volume and enabling regeneration, DCIH converters have been proposed by judiciously combining PCSos and DCVMR. The voltage that the PCSo part needs to handle is reduced by adding a DCVMR part at the output. The DCVMR contains coupled inductor which provides a large conversion ratio using the duty cycle of the switches and the turns ratio of the windings. Since the voltage on the PCSo is reduced, its volume would be smaller. This paper proposes and demonstrates superior DCIH converter topologies in Sec. II. Sec. IV presents experimental results of proposed converter prototypes which demonstrated extreme conversion ratios of ∼2700X, from an input voltage of a small battery around ∼3 V to an output voltage of ∼8 kV. Sec. V concludes the paper.

II. Architecture and Operation of the DCIH Converter with PCSo of Fig. 1c

A. Operating States of the DCIH Converters

The block diagram of the proposed DCIH converter is shown in Fig. 1b. The DCIH converter can be conceptually divided into two PCSos illustrated in Fig. 1b. PCSo A and B can be anyone among the PCSos of Fig. 1. The PCSo consists of switches S_{a2} (S_{b2}), diodes D_{a1} (D_{b1}), D_{a3} (D_{b3}), and coupled inductor T_a (T_b). PCSo B is operated 180°-out-of-phase compared with PCSo A. PCSos are followed by a DCVMR formed by either a 12NDDCVMR (Figs. 3g, 3h, and 3i) [20], [21] or a 12NLDCVMR (Figs. 3a, 3b, and 3c,) [22]–[24], or a 12NMDCVMR structure (Figs. 3d, 3e, and 3f,) [25]. Interleaved structure at the high current side reduces the conduction loss. insertion of 12N(X)DCVMR reduces No. of turns and insulation requirement of coupled inductors. Switches S_{a5} and S_{b5} provide the return path of the current through DCVMR.

The voltages at the two input nodes of the 12N(X)DCVMR are denoted by v_a and v_b, which are the PCSo A and B output voltages, respectively. Ideally, the waveform of v_a (v_b) is a pulse wave with pulse peak V_a (V_b), pulse valley zero. To have a general method to analyze and compare the 12N(X)DCVMR, a consistent naming convention and indexes for them are used. Let $D_{zn}, C_{zn}, v_{C_{zn}}$ $\forall 1 \leq z \leq 12$ denote the diodes, capacitors, and capacitor voltages respectively for the 12N(X)DCVMR. The negative terminal of 12 flying capacitors is connected to the 12 switching nodes in the 12N(X)DCVMR. v_{zn} denotes the voltage of the common node of D_{zn} and C_{zn}, which is the anode terminal of diode D_{zn} and negative terminal of capacitor C_{zn}. 12NDDCVMR, 12NLDCVMR, and 12NMDCVMR differ in the connections of the positive plate of the 12 flying capacitors.

Tab. III summarizes the operating states of the PCSo, the 12N(X)DCVMR separately, and then the entire DCIH

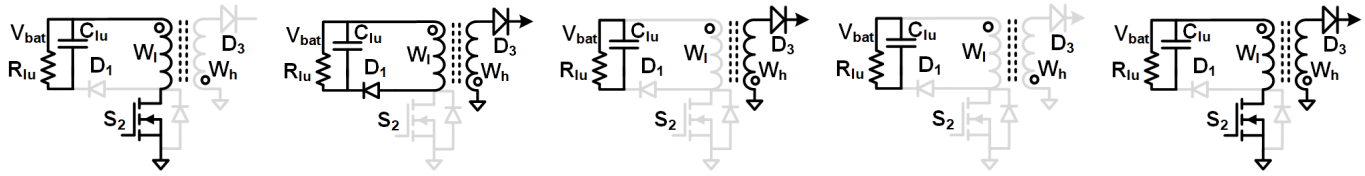

(a) Charging (b) Clamp (c) Discharging (d) Idle (e) Start

Fig. 2. Modes of PCSo of Fig. 1c

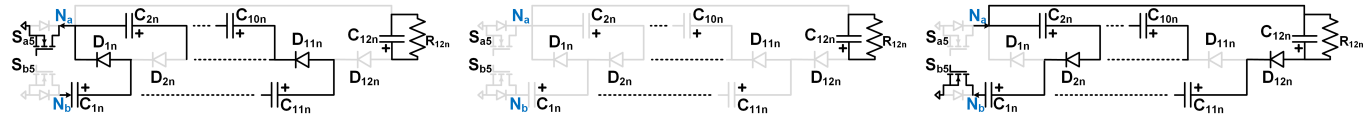

(a) Current enters through N_b of 12NLDCVMR (b) No current enters 12NLDCVMR (c) Current enters through N_a of 12NLDCVMR

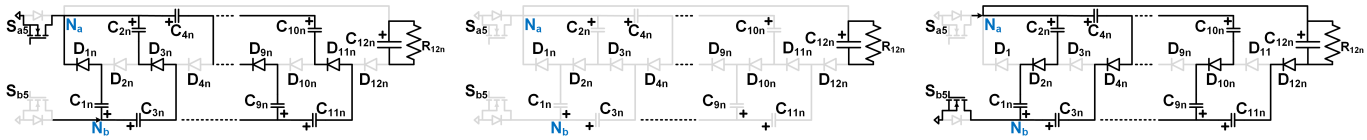

(d) Current enters through N_b of 12NMDCVMR (e) No current enters 12NMDCVMR (f) Current enters through N_a of 12NMDCVMR

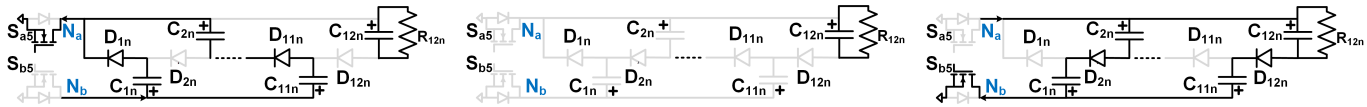

(g) Current enters through N_b of 12NDDCVMR (h) No current enters 12NDDCVMR (i) Current enters through N_a of 12NDDCVMR

Fig. 3. Equivalent circuits describing the operation of the 12N(X)DCVMR part which goes into fitted in Fig.1b

TABLE III
THE OPERATING STATES

PCSo							
PCSo	Fig.	S_1	S_2	D_3	i_m	C_{lu}	Mode
Charging	2a	Off	On	Off	Ch.	Dch.	C & D
Clamp	2b	On	Off	On	Dch.	Ch.	C & D
Discharging	2c	Off	Off	On	Dch.	Dch.	C & D
Idle	2d	Off	Off	Off	-	Dch.	D
Start	2e	Off	On	On	Ch.	Dch.	C & D

12N(X)DCVMR							
State	Fig.	DCVMR					
		S_{a5}	S_{b5}	D_{od}	D_{ev}	C_{od}	C_{ev}
1	3a ‖ 3d ‖ 3g	On	Off	Off	On	Dch.	Ch.
2, 4, 5, 6	3b ‖ 3e ‖ 3h	Off	Off	-	-	-	-
3	3c ‖ 3f ‖ 3i	Off	Off	On	Off	Ch.	Dch.

Proposed DCIH Converters with PCSo of Fig. 1c				
State	PCSo A	PCSo B	12N(X)DCVMR	Mode
1	Fig. 2a	Fig. 2c	Fig. (3a ‖ 3d ‖ 3g)	C & D
2 & 4	Fig. 2c	Fig. 2c	Fig. (3b ‖ 3e ‖ 3h)	C & D
3	Fig. 2c	Fig. 2a	Fig. (3c ‖ 3f ‖ 3i)	C & D
5	Fig. 2a	Fig. 2d	Fig. (3b ‖ 3e ‖ 3h)	D
6	Fig. 2d	Fig. 2a	Fig. (3b ‖ 3e ‖ 3h)	D

*(C-Continuous; D-Discontinuous) Conduction in Column: Mode

converters. Equivalent circuits for PCSos A and B from Fig. 2 combines with the corresponding equivalent circuit from Fig. 3 based on Fig. 5a. One sample of complete DCIH converter operation has been shown in Fig. 4. For this section, the nominal values of the parameters: the turn ratio of the coupled inductor is W_1 (100), the magnetizing inductance is L_m (7.5 μH), the leakage inductance is L_k (0.75 μH), the No. of diodes T (12), the switching period is T_s (50 μS), the duty cycle D (0.65), the resistance across C_{Tn} is R_{Tn} (5 MΩ), the voltage across C_{Tn} is $V_{C_{Tn}}$ (5 kV), and the input voltage of DCIH converter is V_{bat} (3.7 V).

B. Analysis of the DCIH Converters

L_k and the ripple in the capacitor voltages have been neglected to keep the analysis simple. Let the charge delivered by PCSo A (PCSo B) be denoted by Q_a (Q_b) at voltage V_a (V_b). For even T,

$$Q_a = Q_b = \frac{T_s T V_{C_{Tn}}}{2R_{Tn}} \tag{1}$$

$$V_{C_{Tn}} = \frac{T}{2}V_b + \frac{T}{2}V_a \tag{2}$$

For odd T,

$$Q_a = \frac{T_s(T+1)V_{C_{Tn}}}{2R_{Tn}}; Q_b = \frac{T_s(T-1)V_{C_{Tn}}}{2R_{Tn}} \tag{3}$$

$$V_{C_{Tn}} = \frac{T-1}{2}V_b + \frac{T+1}{2}V_a \tag{4}$$

1) Analysis of both PCSo in CCM : The volt-second balance for Figs. 1c, 1f is

$$V_a = V_b = \frac{W_1 D V_{bat}}{1-D} \tag{5}$$

The volt-second balance for Figs. 1d, 1g, 1e, and 1h is

$$V_a = V_b = \frac{(1+W_1 D)V_{bat}}{1-D} \tag{6}$$

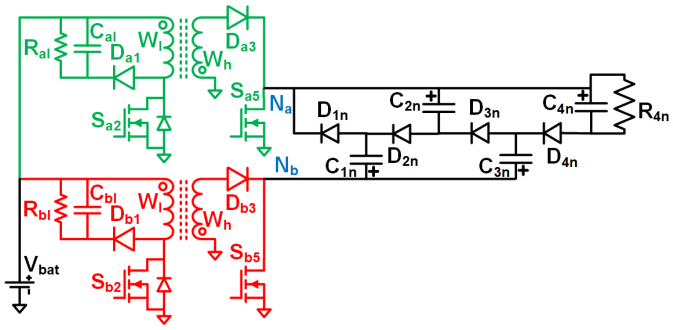

(a) Complete circuit

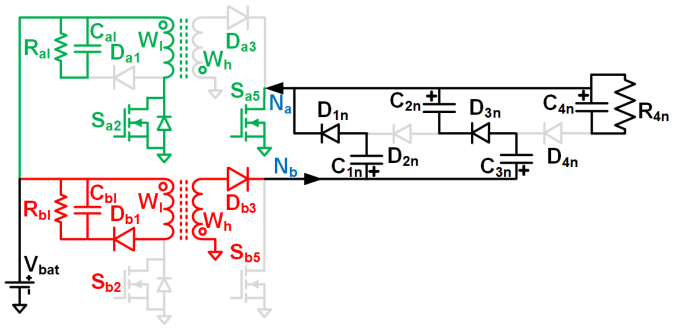

(b) PCSo A charges and PCSo B discharges from $D-0.5$ to 0.5 of Fig. 5a

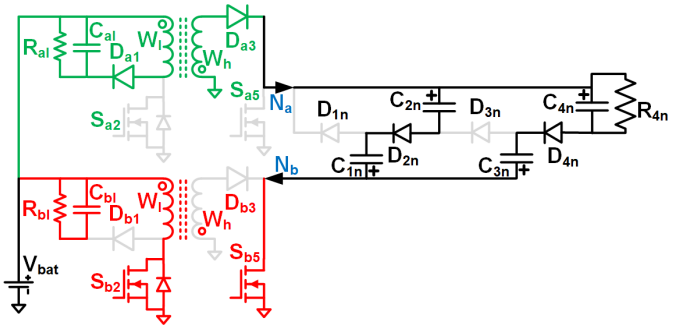

(c) PCSo A discharges and PCSo B charges from D to 1 of Fig. 5a

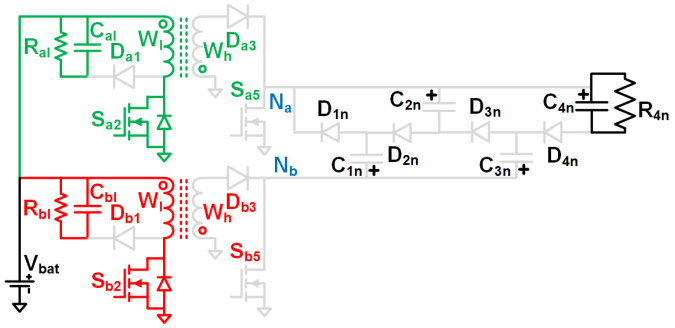

(d) Both PCSos A and B charge from 0 to $D-0.5$ and 0.5 to D of Fig. 5a

Fig. 4. Complete circuit of a sample DCIH converter using Fig. 5a and its operation with a DCVMR with four diodes assuming CCM

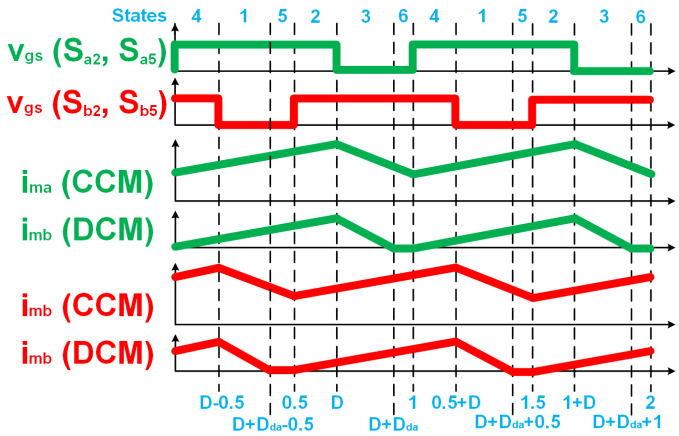

(a) Timing diagram

Fig. 5. Operation of PCSos A and B of the DCIH converter with Fig. 1c

$V_{C_{Tn}}$ for Figs. 1c, 1f is

$$V_{C_{Tn}} = \frac{W_1 D T V_{bat}}{1-D} \tag{7}$$

$V_{C_{Tn}}$ for Figs. 1d, 1g, 1e, and 1h respectively are

$$V_{C_{Tn}} = \frac{(1+W_1 D) T V_{bat}}{1-D} \tag{8}$$

2) Analysis of both PCSo in DCM : The peak of magnetizing current,

$$I_{mp} = \frac{D T_s V_{bat}}{L_m} \tag{9}$$

The volt-second balance for Figs. 1c and 1f in DCM gives the magnetizing current discharge duty cycles of PCSo A (PCSo B) as

$$D_{da} = \frac{W_1 D V_{bat}}{V_a}; D_{db} = \frac{W_1 D V_{bat}}{V_b} \tag{10}$$

Similarly, the volt-second balance for circuits 2, 3, 4, 5, and 6 gives

$$D_{da} = \frac{(1+W_1 D) V_{bat}}{V_a}; D_{db} = \frac{(1+W_1 D) V_{bat}}{V_b} \tag{11}$$

$$\implies \frac{D_{da}}{D_{db}} = \frac{V_b}{V_a} \tag{12}$$

The charge delivered by PCSo A and B in DCM, respectively are

$$\frac{T_s I_{mp} D_{da}}{2W_1} = Q_a; \frac{T_s I_{mp} D_{db}}{2W_1} = Q_b \tag{13}$$

Eq. 12 and Eq. 14 gives

$$\frac{Q_b}{Q_a} = \frac{D_{da}}{D_{db}} = \frac{V_b}{V_a} \tag{14}$$

For even T, Eqs. 14 and 1, gives

$$V_a = V_b = \frac{V_{C_{Tn}}}{T} \tag{15}$$

For odd T, Eqs. 14 and 3, gives

$$\frac{V_b}{V_a} = \frac{T+1}{T-1} \implies V_a = \frac{V_{C_{Tn}}}{T+1}; V_b = \frac{V_{C_{Tn}}}{T-1} \tag{16}$$

If T is even (odd), for Figs. 1c and 1f, solving left equation

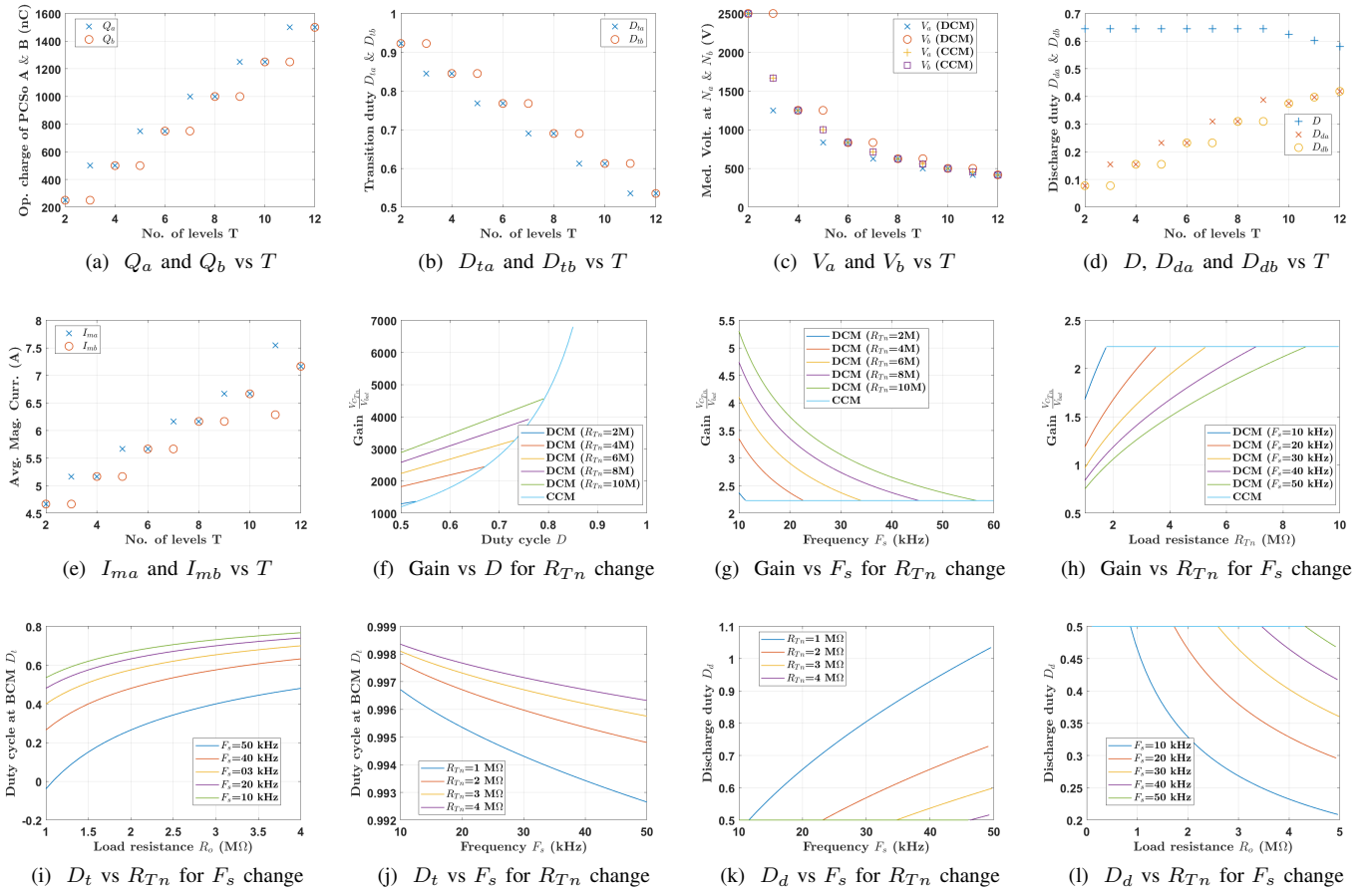

(a) Q_a and Q_b vs T (b) D_{ta} and D_{tb} vs T (c) V_a and V_b vs T (d) D, D_{da} and D_{db} vs T

(e) I_{ma} and I_{mb} vs T (f) Gain vs D for R_{Tn} change (g) Gain vs F_s for R_{Tn} change (h) Gain vs R_{Tn} for F_s change

(i) D_t vs R_{Tn} for F_s change (j) D_t vs F_s for R_{Tn} change (k) D_d vs F_s for R_{Tn} change (l) D_d vs R_{Tn} for F_s change

Fig. 6. Parameter sweeps for proposed DCIH Converters

of Eqs. 13, 9, 10, 15 (16) together, we get

$$V_{C_{Tn}} = DV_{bat}\sqrt{\frac{R_{Tn}T_s}{L_m}} \tag{17}$$

Similarly, If T is even (odd), for Figs. 1d, 1g, 1e, and 1h, solving left equation of Eqs. 13, 9, 11, 15 (16) together, we get

$$V_{C_{Tn}} = \sqrt{\frac{R_{Tn}T_sD}{L_m} \times \frac{1+W_1D}{1+W_1}}V_{bat} \tag{18}$$

3) Mode Transition Duty Cycles : For even T, at the transition boundary between the CCM and DCM, at duty cycle, $D = D_{ta} = D_{tb}$, the voltage gain from DCM and CCM-based analysis can be equated.

for Figs. 1c and 1f,

$$\frac{TW_1D_{ta}V_{bat}}{1-D_{ta}} = D_{ta}V_{bat}\sqrt{\frac{R_{Tn}T_s}{L_m}} \tag{19}$$

$$\implies D_{ta} = D_{tb} = 1 - \sqrt{\frac{L_mT^2W_1^2}{R_{Tn}T_s}} \tag{20}$$

For Figs. 1d, 1g, 1e, and 1h,

$$\frac{T(1+W_1D_{ta})}{1-D_{ta}} = D_{ta}\sqrt{\frac{R_{Tn}T_sD_{ta}}{L_m} \times \frac{1+W_1D_{ta}}{1+W_1}} \tag{21}$$

For $W_1 >> 1$, $1 + W_1D_{ta} \approx W_1D_{ta}$, and $1 + W_1 \approx W_1$. With these substitutions, the above equation can be solved to obtain

$$D_{ta} = D_{tb} \approx 1 - \sqrt{\frac{L_mT^2W_1(1+W_1)}{R_{Tn}T_s}} \tag{22}$$

For odd T, PCSo A reaches CCM early at a duty cycle, $D = D_{ta}$, PCSo B reaches CCM late at a duty cycle, $D = D_{tb}$. Below $D = D_{ta}$, both PCSos stay in DCM. between $D = D_{ta}$ and $D = D_{tb}$ PCSo A stays in CCM and PCSo B stays in DCM. Above $D = D_{tb}$, both PCSos stay in CCM.

For Figs. 1c and 1f,

$$V_a = \frac{1}{T+1}\sqrt{\frac{R_{Tn}T_s}{L_m}}D_{ta}V_{bat} = \frac{W_1D_{ta}V_{bat}}{1-D_{ta}} \tag{23}$$

$$\implies D_{ta} = 1 - \sqrt{\frac{L_m(T+1)^2W_1^2}{R_{Tn}T_s}} \tag{24}$$

$$V_b = \frac{1}{T-1}\sqrt{\frac{R_{Tn}T_s}{L_m}}D_{tb}V_{bat} = \frac{W_1D_{tb}V_{bat}}{1-D_{tb}} \tag{25}$$

$$\implies D_{ta} = 1 - \sqrt{\frac{L_m(T-1)^2W_1^2}{R_{Tn}T_s}} \tag{26}$$

Similarly, for Figs. 1d, 1g, 1e, and 1h,

$$D_{ta} \approx 1 - \sqrt{\frac{L_m(T+1)^2 W_1(1+W_1)}{R_{Tn}T_s}} \tag{27}$$

$$D_{tb} \approx 1 - \sqrt{\frac{L_m(T-1)^2 W_1(1+W_1)}{R_{Tn}T_s}} \tag{28}$$

Hence, for Figs. 1c and 1f, for $0 \leq D \leq D_{ta}$ Eq. 17 holds, for $D_{tb} \leq D \leq 1$ Eq. 7 holds. For $D_{ta} \leq D \leq D_{tb}$ Eq. 5 holds only for V_a. Eq. 10 holds only for D_{db}. Eq. 13 holds only for Q_b. Eq. 9 holds. These valid equations, along with Eqs. 3, and 4 give

$$V_b = \frac{R_{Tn}T_s D^2 V_{bat}^2}{2L_m(T-1)V_{C_{Tn}}} \tag{29}$$

$$V_{C_{Tn}} = \frac{R_{Tn}T_s D^2 V_{bat}^2}{4L_m V_{C_{Tn}}} + \frac{T+1}{2}\frac{W_1 D}{1-D} \tag{30}$$

The above equation is quadratic in $V_{C_{Tn}}$ and cubic in D, solving which for either of them is difficult. Hence, from here onwards, Subsec. II-B2 equations are used for $D_{ta} \leq D \leq D_{tb}$ for simplicity. The same statement holds for Figs. 1d, 1g, 1e, and 1h. Fig. 6 pictorially represents the equations derived in this Sec. in the form of several parameter sweeps using the nominal values of the other parameters.

III. Design Process

The specifications for a target soft robotic application [16], [17] are listed in Tab. IV. To optimize the design, this Sec. provides multiple design trade-offs and guidelines to achieve an optimal design for an extremely high conversion ratio of ∼2700X. The three DCVMR configurations shown in Figs. 3c, 3f, 3i will be compared to guide DCVMR selection among 12PMDCVMR, 12PLDCVMR, and 12PDDCVMR. The different components used in the DCIH converter are categorized in subsections as follows: A. Main semiconductor devices; B. Coupled inductors; C. R_{lu}; D. Flying capacitors; E. PCB and soldering. Each subsection is organized as follows: 1) Theoretical analysis; 2) Practical challenges followed by the list of selected components.

The analysis in this section provides the mathematical expressions for each component's voltage and current magnitudes. All the mathematical constants used in all the derived expressions are listed in Tab. V. Plugging in numerical values from Tab. IV, the voltage and the current ratings of all the components used in the DCIH converters are calculated. Several components may be available that satisfy these ratings. But, there is a trade-off between parasitic elements, size, and cost. Parasitic elements cause losses and other implementation challenges. Components are chosen carefully keeping all these concerns in mind for the practical implementation of the DCIH converter, supporting the untethered operation with the soft robots.

Once all the components of those five subsections are finalized, an additional subsection presents the detailed theoretical efficiency analysis of all three DCIH converter circuits. This analysis is validated later with the experimental measurements. From the converter operation described in Sec. II, the electrical parameters (voltages and the currents) of the PCSos are found, which are listed in Tab. VI.

TABLE IV
Converter Specifications for Typical Operation

Variable	Symbol	Value
Input voltage (V)	V_{bat}	3.7
Output voltage (kV)	V_o	8
Output power (W)	P_o	20
No. of diodes	T	12
Duty ratio	D	0.75
Switching frequency (kHz)	F_s	20

TABLE V
Constant Parameters

Variable	Symbol	Value
Specific Res. of copper	ρ	1.724×10^{-6} Ωcm
Permeability of air	μ_0	$4\pi \times 10^{-7}$ H/m
Sat. flux density of ferrite	B_m	0.25 T
Window factor	K_u	0.3
Approximate copper loss	P_{cu}	1 W
LV MOSFET on Res.	R_{dsl}	0.58 mΩ
LVW resistance	R_l	7.5 mΩ
LV MOSFET parasitic Cap.	C_{dsl}	3.36 nF
Clamp diode Volt. drop	V_{fl}	1.1 V
HVW Res.	R_h	103 Ω
HV MOSFET on Res.	R_{dsh}	75 Ω
HV MOSFET parasitic Cap.	C_{dsh}	8.6 pF
HV diode forward Volt. drop	V_{fh}	3 V
HV diode Junct. Cap.	C_{ak}	3 pF
HVW parasitic Cap.	C_h	62.5 pF

TABLE VI
Electrical Parameters of the PCSo

Variable description	Expression
Avg. volt. at PCSo Op.	$V_a = \frac{V_o}{T}$
Turn's ratio of coupled inductor	$W_1 = \frac{(1-D)V_a}{DV_{bat}}$
Output charge	$Q = \frac{P_o}{V_o F_s}$
Avg. current at CPG Op.	$I_{ab} = 6QF_s$
Avg. of magnetizing current	$I_m = \frac{W_1 I_{ab}}{1-D}$
Ripple of magnetizing current	$\Delta i_m = 0.05 I_m$
Peak of magnetizing current	$I_{mp} = I_m + \Delta i_m$
RMS of magnetizing current	$I_{mr} = I_m\sqrt{1 + \frac{(\Delta i_m)^2}{3(I_m)^2}}$
RMS of LVW current	$I_l = I_{mr}\sqrt{D}$
RMS of HVW current	$I_h = \frac{I_{mr}\sqrt{1-D}}{W_1}$
Total of RMS current	$I_t = I_l + W_1 I_h$

A. Semiconductor Devices

1) Theoretical Analysis : The electrical parameters of the PCSo are listed in Tab. VI to help determine the rating for the semiconductor devices. The voltage appearing across the 2 diodes of the PCSos, D_{a3}, D_{b3} is $W_1 V_{bat}$. The voltage rating of the diode D_{12} is V_a, while it is $2V_a$ for the remaining 11 diodes of the DCVMRs. D_{a3} and D_{b3} each handles $6I_o$ and all other diodes handle I_o. For example, when selecting switches S_{a2} and S_{b2} their breakdown voltage should be larger than $V_x = V_{bat} + \frac{V_a}{W_1} + V_{os}$, where V_{os} is an overshoot voltage allowed on top of the nominal voltage, $V_{bat} + \frac{V_a}{W_1}$. On the HVW side, S_{a5} and S_{b5} need to PCSo a voltage of $\sim 1.2\frac{V_o}{T}$, where the 1.2X factor accounts for the difference between the

peak and the mean of the V_a due to the finite capacitance of the DCVMR.

2) Practical Challenges : It is desirable to select devices with low conduction loss, i.e., low on-resistance, at the input LVW side with low-voltage high-current operation while selecting ones with low switching loss, i.e., low parasitic capacitance, at the high-voltage low-current output side. While this is a general rule in selecting the components, it is crucial to find their constraints. The LVW side switches S_{a2} and S_{b2} only handle small voltages; hence, they do not need a small parasitic drain to source capacitance. However, because of the high current operation, they need to have minimal parasitic on-state resistance for this application. The output switches S_{a5} and S_{b5} only handle small currents; hence, they do not need small on-resistance. However, because of the high operating voltage, it is difficult to find a switch with a small size and small parasitic capacitance for this application. Based on these constraints, the semiconductor devices of the converter are selected as shown in Tab. IX.

B. Coupled Inductors

1) Theoretical Analysis : The electrical parameters of the PCSo are listed in Tab. VI to help determine the rating for the coupled inductors in Tab. VII. Allocation of the window area has been done to minimize the total conduction loss [26]. Considering these trade-offs and design constraints and using the expressions listed in Tab. VII.

TABLE VII
COUPLED INDUCTOR PARAMETERS

Variable description	Expression
Mag. Ind. at LVW	$L_m \approx \frac{V_{bat}D}{2F_s\Delta i_m}$
Leak. ind. at LVW	$L_k \approx 0.05L_m$
Leak. energy at LVW	$P_l \approx 0.05L_kI_{mp}^2$
Geometrical constant	$K_g \approx \frac{\rho L_m^2 I_t^2 I_{mp}^2}{B_m^2 P_{cu} K_u}$
Air gap	$l_g \approx \frac{\mu_0 L_m I_{mp}^2}{B_m^2 A_c}$
No. of LVW turns	$W_l \approx \frac{L_m I_{mp}}{B_m A_c}$
No. of HVW turns	$W_h \approx W_1 W_l$
Fraction of window area allocated for LVW; (HVW)	$a_l \approx \frac{I_l}{I_t}$; $(a_h \approx \frac{I_h}{I_t})$
Cross-sectional area of LVW; (HVW)	$A_{wl} \approx \frac{a_l K_u W_a}{W_l}$; $(A_{wh} \approx \frac{a_h K_u W_a}{W_h})$
DC resistance of LVW; (HVW)	$R_l \approx \frac{\rho l_c W_l}{A_{wl}}$; $(R_h \approx \frac{\rho l_c W_h}{A_{wh}})$
Ripple in flux density	$\Delta B \approx \frac{DV_{bat}}{2F_s N_l A_c}$
Core loss per unit volume	K_{fe} (function of ΔB and F_s)

*Core cross-sectional area (A_c); Window area (A_w); Mean length per turn of winding (l_c); Mean length of magnetic path (l_m)

2) Practical Challenges : Although the DCVMR relaxes the high voltage conversion stress on the coupled inductors, designing them still has significant challenges. A key design challenge is a trade-off between optimizing for low conduction and core losses while supporting high voltages at the secondary side, high currents at the primary side, and maintaining the current saturation limit within a size constraint. Particularly, large magnetizing inductance can lower current ripple to reduce core and conduction losses [26]. However, it can also require more turns in both primary and secondary sides, and hence, larger bobbin and core [27], [28], which increase overall size as well as DC resistance and conduction loss. Many turns also result in multiple layers of winding arrangement which incur a significant amount of proximity loss [26], [29]. Note that interleaving of primary and secondary turns does not help for coupled inductors because current does not flow through the primary (low voltage) and secondary (high voltage) windings simultaneously and there is no flux cancellation benefit. To enable high switching frequency for smaller sizes while still utilizing the winding cross-sectional area, Litz wire, which consists of many small strands of wire, each having a radius close to skin depth has been used to implement the coupled inductors [30]. The primary winding must handle large input currents with a larger total cross-sectional area to reduce its resistance. In the design of these coupled inductors, the secondary needs to produce a high voltage, $\sim 1kV$. Hence, reasonably thick inter-winding and intra-winding insulation must be provided to eliminate the possibility of voltage breakdown in the coupled inductors [31]–[33]. In addition, their printed circuit board (PCB) footprint needs to have enough creepage and clearance distances for high voltage protection related to the secondary pins.

3) Selected Parts : Keeping these concerns in mind the following coupled inductors are chosen. EF-25 core-based coupled inductors were designed and manufactured with a 1:100 turn ratio. Insulating materials capable of withstanding 1.7 kV were placed between the primary and secondary winding layers. 16 mm of separation between the two secondary terminal pins and 20 mm separation between the one primary and one secondary terminal pins are much higher than the required creepage distance for this voltage. The chosen insulation structure resulted in 80 pF parasitic capacitance. Due to high current flow in the LVW, two primary windings each made up of 8 turns of 40 strands of 36 AWG Litz wire are connected in parallel to reduce the winding DC and AC resistance. Due to the high voltage requirement of the HVW, two secondary windings each made up of 387 turns of only 1 strand of 40 AWG Litz wire are connected in series. The working temperature range of the coupled inductor is -40 ^{o}C to 85 ^{o}C. This winding design results in 7.5 mΩ and 103 Ω DC resistances for LVW and HVW respectively. EF-25 core is used which accommodates the entire winding structure. An MnZn-based ferrite material with high permeability and reasonably high resistivity is used to prevent eddy currents at a high frequency. The chosen core structure with the selected winding turns resulted in a magnetizing inductance of 7.5 uH, and 0.5 uH leakage inductance. The designed coupled inductor can have a 20 A saturation current and 20 W power rating.

C. Selection of R_{lu} and C_{lu}

1) Theoretical Analysis : Practically, finite L_k causes the voltage ratings of S_{a2}, D_{a1} to rise very high. Hence, resistor R_{lu} is placed in parallel to C_{lu} to keep the LV device voltage rating within the desired limit. Suppose the allowed voltage

overshoot of LV switches (V_{os}) is 50% of the nominal voltage of the switches

$$V_{os} \approx 0.5(V_{bat} + \frac{V_a}{W_1}) \tag{31}$$

The capacitor C_{lu} voltage is $V_{C_{lu}}$

$$V_{C_{lu}} \approx \frac{V_a}{W_1} + V_{os} \tag{32}$$

If $T_{D_{a1}}$ is the conduction time and $Q_{D_{a1}}$ is the conducted charge of D_{a1}, then the resistor R_{lu} is

$$R_{lu} \approx \frac{V_{C_{lu}}}{F_s Q_{D_{a1}}} = \frac{T_s V_{C_{lu}}}{0.5 I_{mp} T_{D_{a1}}} = \frac{2T_s V_{C_{lu}} V_{os}}{L_k I_{mp}^2} \tag{33}$$

The power loss of R_{lu} is P_{cr} is

$$P_{cr} \approx \frac{V_{C_{lu}}^2}{R_{lu}} = \left(\frac{V_a}{W_1 V_{os}} + 1\right) \frac{1}{2} L_k I_{mp}^2 \tag{34}$$

2) Practical Challenges : Eqs. 33, 31, 32 give V_{os}, $V_{C_{lu}}$, R_{lu}, which says that for higher V_{os}, $V_{C_{lu}}$ must be higher. $T_{D_{a1}}$ is high if L_k and I_{mp} are high. P_{cr} increases if V_{os} decreases. This means if a switch of low voltage rating (resulting in small size and low conduction loss) is chosen, higher loss occurs across R_{lu}. Generally, $V_{os} < V_{bat} + \frac{V_a}{W_1}$. Hence, $P_{cr} > 0.5 L_k I_{mp}^2$.

D. Flying Capacitors

1) Theoretical Analysis : The theoretical analysis of average capacitor voltages is presented in Tab. VIII.

TABLE VIII
CHARGE MULTIPLICATION FACTORS AND AVERAGE VOLTAGES OF FLYING CAPACITORS OF THE 12N(X)DCVMR

Cap.	$\frac{q_{C_i}}{Q}$ if X is			$\frac{V_{C_i}}{V_b}$ if X is		
C_{in}	L	M	D	L	M	D
C_{1n}	6	1	1	1	1	1
C_{2n}	5	1	1	2	2	2
C_{3n}	5	5	1	2	3	3
C_{4n}	4	4	1	2	4	4
C_{5n}	4	1	1	2	2	5
C_{6n}	3	1	1	2	2	6
C_{7n}	3	3	1	2	4	7
C_{8n}	2	2	1	2	4	8
C_{9n}	2	1	1	2	2	9
C_{10n}	1	1	1	2	2	10
C_{11n}	1	1	1	2	4	11
C_{12n}	1	1	1	12	12	12

*Q is charge transferred to the load resistance over a switching period; V_b is the peak of the pulsed voltage at node N_b

2) Practical Challenges :

a) Size : The theoretical analysis of average capacitor voltages presented in Tab. VIII shows that the capacitors of 12PDDCVMR operate at different voltages that increase in arithmetic progression from lower to higher indexes. The capacitors near the output must be rated for extremely high voltages, close to the output voltage. Only through-hole ceramic disc capacitors with bulky packages are available at this extremely high voltage rating. Moreover, this type of capacitor is only available with limited and relatively small capacitance values. Hence, the weight and volume of 12PDDCVMR are higher than those of 12PLDCVMR and 12PMDCVMR. On the other hand, all 12PLDCVMR capacitors operate at or lower than twice the PCSo output voltage, $2V_a$, which is a small fraction of the output voltage, $\frac{V_o}{6}$. This enables the use of relatively lower voltage capacitors that are available in smaller packages (surface mount type) and higher capacitance values. Therefore, scaling up 12PLDCVMR for a higher output voltage is much easier and theoretically implies linear area and weight increase. Hence, 12PLDCVMR can be implemented with a small volume and weight.

E. PCB Design and Soldering

High-voltage circuits require additional precautions to ensure reliable operation due to the potential risks associated with high-voltage breakdown. The objective is to limit the electric field intensity below the breakdown strength of the insulating material, which is achieved by increasing the radius of curvature of all points on the conductors and increasing the separation between the points having voltage differences.

PCB Layout: High-voltage PCB design guidelines, such as maintaining adequate clearances and creepage distances between high-voltage conductors and other components, must be followed meticulously. High-voltage traces must be well-insulated and kept away from low-voltage components. Sharp corners in the traces and pads should be completely avoided.

Soldering Iron: The soldering iron's power rating and tip size must be appropriate for the specific components and leads.

Cleanliness: The components and PCB must be cleaned before soldering, using isopropyl alcohol or a specialized electronics cleaner to remove any contaminants, residues, or oxidation that may affect the soldering process.

Heat Control: The heat applied during soldering must be controlled to prevent excessive heating of the components. High temperatures can damage or degrade the components, affecting their performance or even causing them to fail.

Soldering Technique: Following standard soldering techniques must be applied:

a. Pre-tinning the Components: A thin solder layer must be applied to the component leads before soldering to facilitate proper solder flow and connection.

b. Application of the Right Amount of Solder: An appropriate amount of solder must be used to form a reliable and robust joint. Using excessive solder must be avoided because it can cause bridging or short circuits. The desired shape of the solder joints is a smooth rounded ball.

c. Quick Soldering: The exposure of the components to the heat must be minimized by completing the soldering process as quickly as possible. Prolonged heat exposure can damage sensitive high-voltage components.

d. Avoiding Excess Flux: Only the necessary amount of flux must be used to ensure proper solder wetting and avoid excessive flux residues that can cause contamination or electrical leakage.

TABLE IX
MAJOR COMPONENTS

Major Components without Flying Capacitors	
Part Name	Part No.
Micro-controller	TMS320f28379D
Half-bridge gate driver	UCC27201DR6
Low-side gate driver	IX4427NTR
Decoupling capacitor	C0805C105K3RAC7210
Bootstrap capacitor	C0805C104K3RACTU
C_{alu}, C_{blu}	C2012X5R1V226M125AC
R_{alu}, R_{blu}	HRG3216P-1000-B-T1
$S_{a1}, S_{a2}, S_{b1}, S_{b2}$	SIRA20DP-T1-RE3
T_a, T_b	XF0757-EF25R-A
D_{a3}, D_{b3}	GAP3SLT33-214
S_{a5}, S_{b5}	IXTY02N120P
$D_1, D_2, ..., D_{12}$	GP02-40-E3/73
C_o	HVCC153Y6P202MEAX

Flying Capacitors of the 12N(X)DCVMR		
If X is	Part Name	Part No.
L	$C_1, C_2, ..., C_{11}$	HV2225Y332KXMATHV
M	$C_1, C_2, C_5, C_6, C_9, C_{10}$	2225WC223KAT1A
	$C_3, C_4, C_7, C_8, C_{11}$	HV2225Y332KXMATHV
D	C_1, C_2	2225WC223KAT1A
	C_3, C_4	HV2225Y332KXMATHV
	$C_5, C_6, ..., C_{11}$	HVCC153Y6P202MEAX

F. Power Loss and Efficiency

Once all the components are finalized, then all the parasitic elements related to the different components are listed in Tab. V. Based on this analysis, the efficiencies for different DCIH converters for different operating conditions can be estimated. The peak of V_a and V_b are found using the equivalent capacitance of these nodes, which are used along with the parasitic elements listed in Tab. V, the individual loss components are estimated and listed in Tab. X. Individual loss components are plotted as a pi chart for a better pictorial representation. This theoretical efficiency analysis sows higher efficiencies with the 12PDDCVMR-based converter which is again extensively validated later through the experimental measurements.

TABLE X
INDIVIDUAL LOSS COMPONENTS

Variable Description	Expression
Loss of R_{lu}	$P_{cr} \approx 2 \times \frac{P_l V_c}{V_{os}}$
Cond. loss of D_{a1}, D_{a2}	$P_{cdc} \approx 2 \times V_{fl} Q_c F_s$
Cond. loss of 2 LVW	$P_{cwl} \approx 2 \times I_l^2 R_l$
Cond. loss of S_{a2} and S_{b2}	$P_{cml} \approx 2 \times I_l^2 R_{dsl}$
Sw. loss of D_{a1}, S_{a2}, D_{b1}, S_{b2}	$P_{sml} \approx 4 \times 0.5 C_{dsl} V_c^2 F_s$
Cond. loss of 2 HVW	$P_{cwh} \approx 2 \times I_l^2 R_h$
Cond. loss of S_{a5} and S_{b5}	$P_{cmh} \approx 2 \times I_h^2 R_{dsh}$
Sw. loss of S_{a5} and S_{b5}	$P_{smh} \approx 2 \times 0.5 C_{dsh} V_a^2 F_s$
Hard discharge loss of 2 HVW	$P_{sth} \approx 2 \times 0.5 C_h V_a^2 F_s$
Cond. loss of diodes D_1 to D_{12}	$P_{cd1} \approx 12 \times V_{fh} Q F_s$
Cond. loss of D_{a3} and D_{b3}	$P_{cd2} \approx 2 \times 6 V_{fh} Q F_s$
Sw. loss of D_1 to D_{11}	$P_{sd1} \approx 11 \times 4 C_{ak} V_a^2 F_s$
Sw. loss of D_{12}	$P_{sd2} \approx C_{ak} V_a^2 F_s$
Coupled inductor core loss	$P_{fe} \approx k_{fe} A_c l_m$

It is important to recognize that complete soft-charging is achieved for all these three DCVMRs because each diode only allows unidirectional currents and only gets on when the voltage difference between its anode and cathode node becomes zero. The output voltage of the converters is the same when the load resistance and output power are the same. For an example, for $T = 12$ $\forall C - z = C$, the effective capacitance at node N_b of the 12NDDCVMR, 12NMDCVMR and 12NLDCVMR are $3C$, $\frac{15C}{14}$ and $\frac{7C}{13}$ respectively. As a result, for the same median voltage of v_b, the 12NLDCVMR has a higher peak voltage V_p than 12NDDCVMR. As a result, compared to the 12NDDCVMR, the 12NLDCVMR has significantly more switching losses and impulse discharging losses due to the parasitic capacitance of the HVW (C_h). As a result, the 12NLDCVMR DCIH converter performs less efficiently than the 12NDDCVMR DCIH converter. The three converters' efficiency differences agree with the observations in Fig. 11. The converters' loss divisions are computed and shown in Fig. 7. The sum of all tabulated individual losses represents the approximate total loss of the converter and is indicated by P_{loss}. Converter efficiency is $\eta = \frac{P}{P+P_{loss}}$. It can be observed from Fig. 10 that a lower current causes the high-resistance LVW to suffer less conduction loss, allowing for higher efficiency at reduced duty cycles.

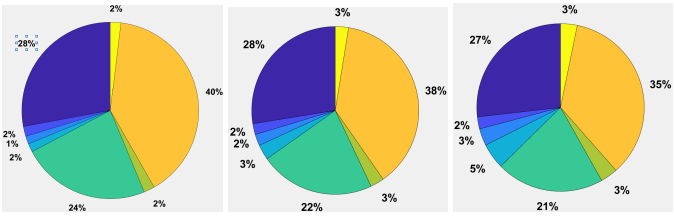

(a) 68 % efficiency with 12NLDCVMR (b) 74 % efficiency with 12NMDCVMR (c) 78 % efficiency with 12NDDCVMR

(d) Legends (some minor losses are combined together in pairs)

Fig. 7. Power loss components of DCIH converters with the 12N(X)DCVMR for 15 W output power and 8 kV output voltage at 20 kHz switching frequency

Although 12PLDCVMR can benefit from higher capacitance values to improve its voltage drop and efficiency, as will be shown in Sec. IV, it still has the lowest efficiency even with the largest capacitance available for its operation because of significant voltage drops. Being a hybrid between the two configurations 12PDDCVMR and 12PLDCVMR, 12PMDCVMR achieves the performance and size trade-off. A comparative study between the fabricated DCIH converters with these three DCVMR configurations is presented in Sec. IV. Keeping these concerns in mind, the flying capacitors of the DCVMRs are chosen which are listed in Tab. IX.

IV. DEMONSTRATION OF THE PROPOSED DCIH CONVERTER WITH PCSO OF FIG. 1C

The proposed DCIH converter architecture has been demonstrated using three experimental prototypes of the DCIH converter shown in Figs. 9a 8a, 8b, and 8c which implements three configurations for the 12N(X)DCVMR using the components listed in Tab. IX.

Different capacitor voltage and switching node voltage waveforms are captured during the steady-state operation of the converter in an open loop. Two high-voltage probes

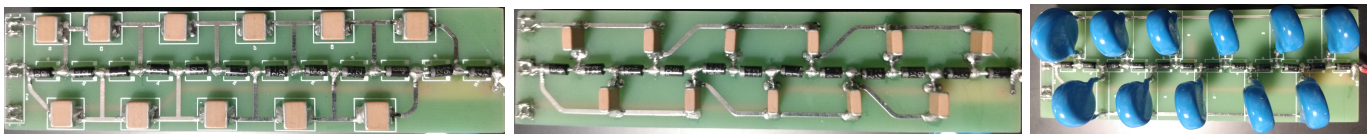

(a) 12NLDCVMR prototype (b) 12NMDCVMR prototype (c) 12NDDCVMR prototype

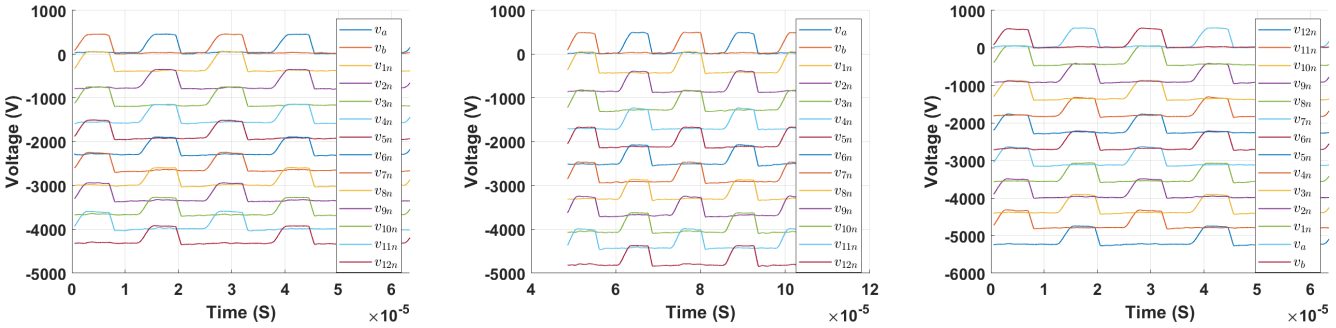

(d) Node voltages of 12NLDCVMR (e) Node voltages of 12NMDCVMR (f) Node voltages of 12NDDCVMR

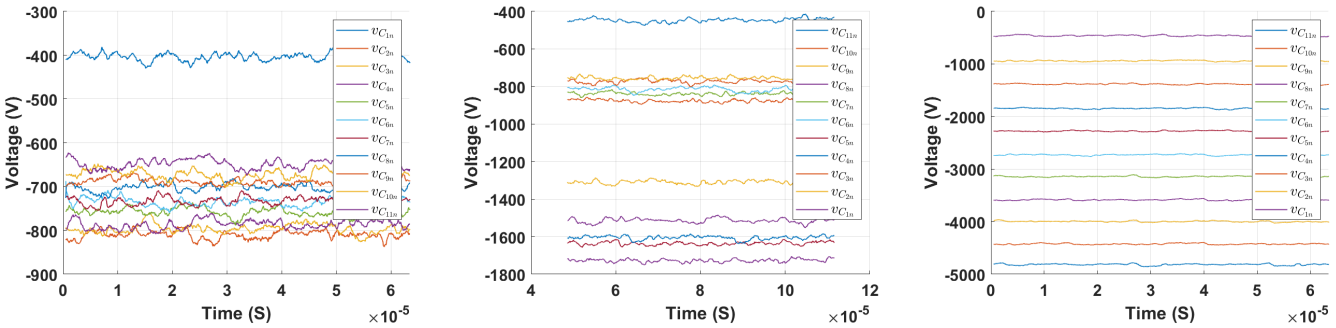

(g) Capacitor voltages of 12NLDCVMR (h) Capacitor voltages of 12NMDCVMR (i) Capacitor voltages of 12NDDCVMR

Fig. 8. Measured node voltage, and capacitor voltage waveforms of the 12N(X)DCVMR with 50 MΩ

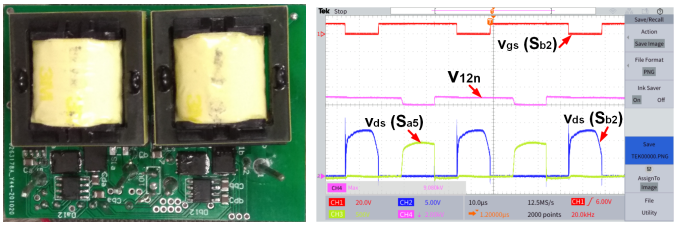

(a) Prototype of PCSo (b) Waveforms of 12NDDCVMR

Fig. 9. Prototype of PCSo and its Exp. waveforms with the 12NDDCVMR

measuring up to 15 kV are used to capture capacitor and output voltages, each offering a high input resistance of 100 MΩ. However, because the currents of the components on the high voltage side are minimal and they are at a dangerously high voltage, measuring these values precisely and safely with the available current sensors is very challenging.

The operations of the PCSo are verified in Fig. 9b. $v_{gs}(S_{b2})$ and $v_{ds}(S_{b2})$ are the gate-source and drain-source voltages of the switch S_{b2}. $v_{ds}(S_{b2})$ waveform illustrates no excessive voltage spike, validating the intended functionality of the R_{lu}. The voltage waveform at the input node of 12N(X)DCVMR N_a ($v_{ds}(S_{a5})$) only reaches a small fraction of the output voltage, approximately $\frac{V_{C_{Tn}}}{T}$, reducing the No. of turns and insulation requirement of the coupled inductor.

All node voltages of the 12N(X)DCVMR with a load resistance of 50 MΩ are provided in Figs. 8d, 8e, and 8f. All capacitor voltages $v_{C_{zn}}$ $\forall 1 \leq z \leq 12$ of the 12N(X)DCVMR are provided in Figs. 8g, 8h, and 8i, which were estimated in Tab. VIII. $V_{C_{12n}}$ is the output voltage, the voltage difference between nodes V_{12n} and N_a. Fig. 12a shows the experimental setup of the proposed converter with HASEL. Fig. 12b (Fig. 12c) shows the actuation waveforms of HASEL actuator at 1 (2) Hz with a discharge resistance R_{Tn} of 5 MΩ which discharges the HASEL actuator C_{Tn}.

TABLE XI
COMPARISON OF THE VOLUME, WEIGHT, COST, AND EFFICIENCY OF THE IMPLEMENTED DCIH CONVERTERS WITH THE 12N(X)DCVMR

If X is	Flying caps			All components			P	E
	V	W	C	V	W	C	V	
L	1	5.39	16	40.5	122	54.3	90	65
M	1	7.37	16	40.5	125	57.5	113	68
D	0.976	49.6	21	55.7	167	62.6	203	75

*V-Volume (cm^3); W-Weight (g); C-Cost (USD); P-Packaging with enclosure; E-Efficiency

Finally, comparisons among 12N(X)DCVMR-based DCIH converters have been presented in Tab. XI, which shows that while the 12NDDCVMR-based prototype has superior

This article has been accepted for publication in IEEE Journal of Emerging and Selected Topics in Industrial Electronics. This is the author's version which has not been fully edited and content may change prior to final publication. Citation information: DOI 10.1109/JESTIE.2023.3302704

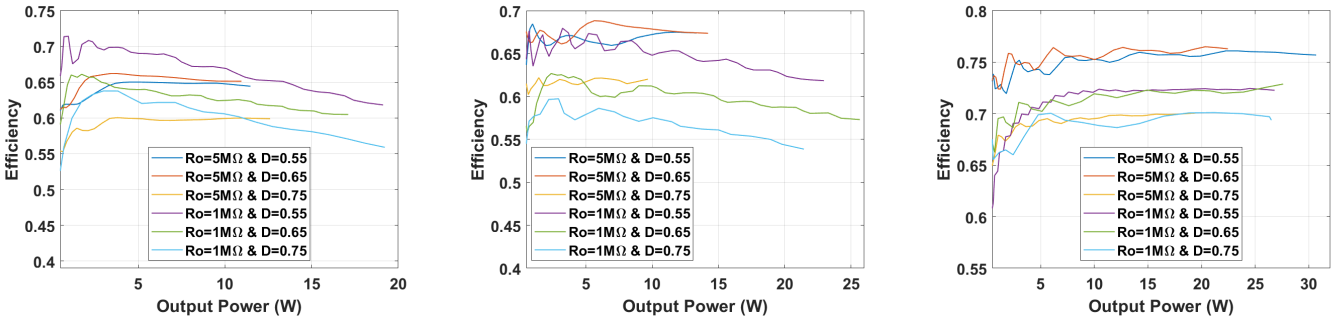

(a) 12NLDCVMR (b) 12NMDCVMR (c) 12NDDCVMR

Fig. 10. Experimental measured efficiencies with open-loop operations of the DCIH converter prototypes (Figs. 9a 8a, 8b, and 8c) with variable input voltages resulting in variable power output for different loading conditions (5MΩ and 1MΩ) and different duty cycles (0.55, 0.65 and 0.75) with different DCVMRs.

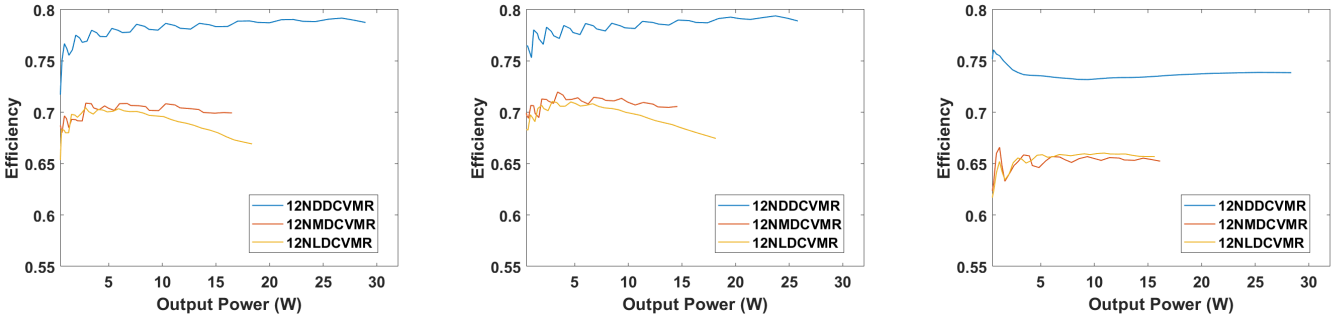

(a) D=0.5 (b) D=0.6 (c) D=0.7

Fig. 11. Measured performances of the DCIH converter prototypes (Fig. Figs. 9a 8a, 8b, and 8c) in open-loop operations with variable input voltages resulting in variable power output for different duty cycles when supplying 2.5 MΩ load resistance.

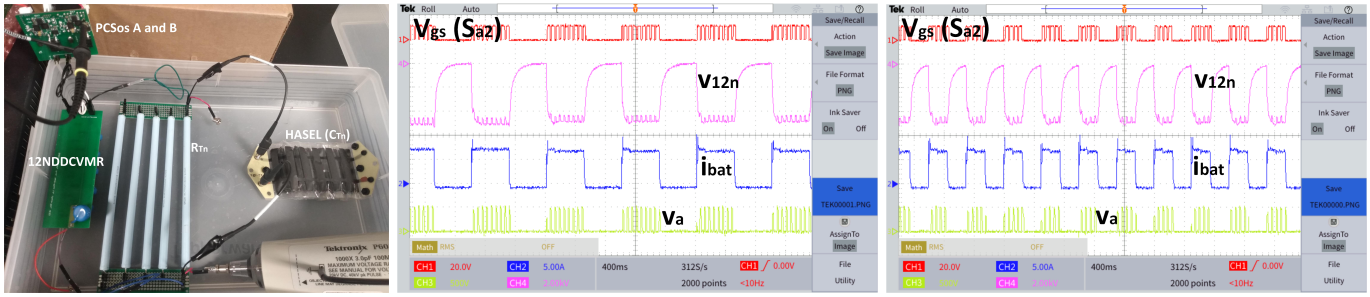

(a) Exp. setup with HASEL (b) Actuation of HASEL at 1 Hz (c) Actuation of HASEL at 2 Hz

Fig. 12. Actuation of HASEL

efficiency, the 12NLDCVMR has a smaller size and smaller weight, and the 12NMDCVMR can give a reasonable compromise between efficiency and size. Comparisons of the 12NDDCVMR-based DCIH converter with similar commercial products have been presented in Tab. II which proves the superiority of the proposed DCIH converters in terms of output power, power density, and adjustable output voltage capability. Tab. I shows that high gain converters demonstrated in the literature are unsuitable for actuating HASEL.

V. CONCLUSIONS

In this paper, DCIH converter topologies are proposed with their operation, analysis, and experiment results, demonstrating a promising solution for soft mobile robots. Thanks to the efficient synchronous operation between compact PCSos and 12N(X)DCVMR. The proposed converters can support a huge conversion ratio of ∼2700X while achieving high efficiency, high output power, and adjustable output voltage in a compact size. Multiple converter prototypes were implemented, and their performances were compared to provide parameter tradeoffs and design directions. The demonstration results and comparisons prove the proposed converter is an excellent candidate for driving HASEL actuator-based soft mobile robots.

REFERENCES

[1] N. Kellaris, V. Gopaluni Venkata, G. M. Smith, S. K. Mitchell, and C. Keplinger, "Peano-hasel actuators: Muscle-mimetic, electrohydraulic transducers that linearly contract on activation," *Science Robotics*, vol. 3, no. 14, p. eaar3276, 2018.

[2] X. Wang, S. K. Mitchell, E. H. Rumley, P. Rothemund, and C. Keplinger, "High-strain peano-hasel actuators," *Advanced Functional Materials*, vol. 30, no. 7, p. 1908821, 2020.
[3] A. Robotics, "Application areas of HASEL actuators." [Online]. Available: https://www.artimusrobotics.com/
[4] T. Kim, S. J. Yoon, and Y.-L. Park, "Soft inflatable sensing modules for safe and interactive robots," *IEEE Robotics and Automation Letters*, vol. 3, no. 4, pp. 3216–3223, 2018.
[5] L. Somm, D. Hahn, N. Kumar, and S. Coros, "Expanding foam as the material for fabrication, prototyping and experimental assessment of low-cost soft robots with embedded sensing," *IEEE Robotics and Automation Letters*, vol. 4, no. 2, pp. 761–768, 2019.
[6] K.-B. Park, G.-W. Moon, and M.-J. Youn, "Nonisolated high step-up stacked converter based on boost-integrated isolated converter," *IEEE Transactions on Power Electronics*, vol. 26, no. 2, pp. 577–587, 2010.
[7] K.-C. Tseng and C.-C. Huang, "High step-up high-efficiency interleaved converter with voltage multiplier module for renewable energy system," *IEEE transactions on industrial electronics*, vol. 61, no. 3, pp. 1311–1319, 2013.
[8] W. Li, X. Xiang, C. Li, W. Li, and X. He, "Interleaved high step-up zvt converter with built-in transformer voltage doubler cell for distributed pv generation system," *IEEE Transactions on Power Electronics*, vol. 28, no. 1, pp. 300–313, 2012.
[9] S.-M. Chen, T.-J. Liang, L.-S. Yang, and J.-F. Chen, "A boost converter with capacitor multiplier and coupled inductor for ac module applications," *IEEE Transactions on industrial Electronics*, vol. 60, no. 4, pp. 1503–1511, 2011.
[10] T.-F. Wu, Y.-S. Lai, J.-C. Hung, and Y.-M. Chen, "Boost converter with coupled inductors and buck–boost type of active clamp," *IEEE Transactions on Industrial Electronics*, vol. 55, no. 1, pp. 154–162, 2008.
[11] P. Electronics, "Series AVP and AVN plug-in DC-DC converters." [Online]. Available: https://www.picoelectronics.com/node/68748
[12] PICO, "SERIES: VV,VV-P,VV-N | Pico." [Online]. Available: https://www.picoelectronics.com/node/13288
[13] EMCO, "Isolated, proportional DC to HV DC converters, 100V to 10000V @ 0.5W." [Online]. Available: https://www.heliosps.com.au/product/q-series-dc-hv-dc-converters-0-5w-emco-xp-power/
[14] X. Power, "XP Power - AG60P-5 - DC-DC Converter; Surface Mount; SMD; 1W; 6000V@167A; 0.7-5V In; AG Series - Allied Electronics & Automation." [Online]. Available: https://www.xppower.com/portals/0/pdfs/SF_AG_Series.pdf
[15] T. Xie, M. R. Oltra, and H.-P. Le, "A 5kv/15w dual-transformer hybrid converter with extreme 2000x conversion ratios for soft mobile robots," in *2020 IEEE Applied Power Electronics Conference and Exposition (APEC)*. IEEE, 2020, pp. 1548–1552.
[16] D. Rus and M. T. Tolley, "Design, fabrication and control of origami robots," *Nature Reviews Materials*, vol. 3, no. 6, pp. 101–112, 2018.
[17] E. Acome, S. K. Mitchell, T. Morrissey, M. Emmett, C. Benjamin, M. King, M. Radakovitz, and C. Keplinger, "Hydraulically amplified self-healing electrostatic actuators with muscle-like performance," *Science*, vol. 359, no. 6371, pp. 61–65, 2018.
[18] K.-C. Tseng, J.-T. Lin, and C.-C. Huang, "High step-up converter with three-winding coupled inductor for fuel cell energy source applications," *IEEE Transactions on Power Electronics*, vol. 30, no. 2, pp. 574–581, 2014.
[19] K.-C. Tseng, J.-Z. Chen, J.-T. Lin, C.-C. Huang, and T.-H. Yen, "High step-up interleaved forward-flyback boost converter with three-winding coupled inductors," *IEEE Transactions on Power Electronics*, vol. 30, no. 9, pp. 4696–4703, 2014.
[20] J. F. Dickson, "On-chip high-voltage generation in mnos integrated circuits using an improved voltage multiplier technique," *IEEE Journal of solid-state circuits*, vol. 11, no. 3, pp. 374–378, 1976.
[21] V. A. K. Prabhala, P. Fajri, V. S. P. Gouribhatla, B. P. Baddipadiga, and M. Ferdowsi, "A dc–dc converter with high voltage gain and two input boost stages," *IEEE Transactions on Power Electronics*, vol. 31, no. 6, pp. 4206–4215, 2015.
[22] L. Müller and J. W. Kimball, "High gain dc–dc converter based on the cockcroft–walton multiplier," *IEEE Transactions on Power Electronics*, vol. 31, no. 9, pp. 6405–6415, 2015.
[23] H. Xu, Y. He, K. L. Strobel, C. K. Gilmore, S. P. Kelley, C. C. Hennick, T. Sebastian, M. R. Woolston, D. J. Perreault, and S. R. Barrett, "Flight of an aeroplane with solid-state propulsion," *Nature*, vol. 563, no. 7732, pp. 532–535, 2018.
[24] G. Mabler, B. Yu, G. Smith, W. Kane, and J. Lemley, "A portable gamma-ray spectrometer using compressed xenon," in *1997 IEEE Nuclear Science Symposium Conference Record*, vol. 1. IEEE, 1997, pp. 769–773.
[25] S. Park, J. Yang, and J. Rivas-Davila, "A hybrid cockcroft–walton/dickson multiplier for high voltage generation," *IEEE Transactions on Power Electronics*, vol. 35, no. 3, pp. 2714–2723, 2019.
[26] R. W. Erickson and D. Maksimovic, *Fundamentals of power electronics*. Springer Science & Business Media, 2007.
[27] F. Semiconductor, "Design guidelines for rcd snubbers of flyback." [Online]. Available: https://www.datasheetarchive.com/pdf/download.php?id=92cda5552c81dfd8087130d05840c02f884f15&type=M&term=AN4147
[28] R. Engineering, "Design, Build and Test a Flyback Transformer - Webinar." [Online]. Available: https://ridleyengineering.com/videos-e/302-design-build-and-test-a-flyback-transformer-webinar.html
[29] W. G. Hurley, E. Gath, and J. G. Breslin, "Optimizing the ac resistance of multilayer transformer windings with arbitrary current waveforms," *IEEE transactions on power electronics*, vol. 15, no. 2, pp. 369–376, 2000.
[30] W. G. Hurley, W. H. Wolfle, and J. G. Breslin, "Optimized transformer design: Inclusive of high-frequency effects," *IEEE transactions on power electronics*, vol. 13, no. 4, pp. 651–659, 1998.
[31] M. S. Naidu and M. K. NAIDU, *High voltage engineering*. Tata McGraw-Hill Education, 2013.
[32] J. Kuffel and P. Kuffel, *High voltage engineering fundamentals*. Elsevier, 2000.
[33] C. Wadhwa, *High voltage engineering*. New Age International, 2006.

Tirthasarathi Lodh received the B.Tech. Degree in Electrical Engineering from Jadavpur University, India, in 2014, and the M. Tech. Degree from the Dept. of Electrical Engineering, I.I.T. Bombay, India, in 2017. He was an Associate Research and Development Engineer at Asea Brown Boveri (ABB) Global Industries and Services Private Limited till 2019. He is a doctoral student at the University of California San Diego, USA. His research interests are high-gain converters and microinverters.

Hanh-Phuc Le received a B.S. degree from the Hanoi University of Science and Technology (HUST), Hanoi, Vietnam, in 2004, the M.S. degree from the Korea Advanced Institute of Science and Technology (KAIST), Daejeon, South Korea, in 2006, and the Ph.D. degree from the University of California at Berkeley, Berkeley, CA, USA, in 2013, all in Electrical Eng. He is currently an Assistant Prof. at the Electrical and Computer Engineering Department, the University of California at San Diego (UCSD), La Jolla, CA, USA.